Facet-Dependent, Fast Response, and Broadband Photodetector Based on Highly Stable All-Inorganic CsCu₂I₃ Single Crystal with 1D Electronic Structure

Ziqing Li, Ziliang Li, Zhifeng Shi,* and Xiaosheng Fang*

Low-dimensional metal halides at molecular level, which feature strong quantum confinement effects from intrinsic structure, are emerging as ideal candidates in optoelectronic fields. However, developing stable and nontoxic metal halides still remains a great challenge. Herein, for the first time, high-crystalline and highly stable CsCu₂I₃ single crystal, which is acquired by a low-cost antisolvent vapor assisted method, is successfully developed to construct high-speed ($t_{rise}/t_{decay} = 0.19$ ms/14.7 ms) and UV-to-visible broadband (300–700 nm) photodetector, outperforming most reported photodetectors based on individual all-inorganic lead-free metal halides. Intriguingly, facet-dependent photoresponse is observed for CsCu₂I₃ single crystal, whose morphology consists of {010}, {110}, and {021} crystal planes. The on–off ratio of {010} crystal plane is higher than that of {110} crystal plane, mainly owing to lower dark current. Furthermore, photogenerated electrons are localized in twofold chains created by [CuI₄] tetrahedra, leading to relatively small effective mass and fast transport mobility along the 1D transport pathway. Anisotropic carrier transport characteristic is related to stronger confinement and higher electron density for {110} crystal planes. This work not only demonstrates the great potential of CsCu₂I₃ single crystal in high-performance optoelectronics, but also gives insights into 1D electronic structure associated with fast photoresponse and high anisotropy.

1. Introduction

Photodetector, which can convert light signals into electrical signals, serves as an important optoelectronic device in many fields such as military, medicine, life, industry, scientific research, and so on.[1] Low-dimensional semiconductor materials have shown attractive prospects for optoelectronics during the past few years. Researchers have been making continuous efforts on exploring nanostructure materials (0D quantum dots, 1D nanowires and nanotubes, 2D nanoplates) and atomically thin 2D materials to prepare high-speed, broadband and sensitive optoelectronic devices to meet the application requirements.[2]

Different from reducing morphology size to several nanometers, low-dimensional semiconductor materials featuring 0D, 1D, 2D structural dimensionality are of great interest to exhibit unique photophysical performances,[3] because of strong quantum confinement effects from crystal structure in nature.[4] Against this background, molecular-level low-dimensional metal halides are arising as ideal candidates in many optoelectronic fields,[5] such as light-emitting diodes, solar cells and lasers. Although organic–inorganic metal halide perovskites demonstrate advantages of structural diversity, tunable band structure and soft crystal lattice,[6] their poor thermal and chemical stabilities are considered as major limiting factors, which are originated from organic cations in the framework.[7] Among all-inorganic metal (Pb, Sn, Bi, Sb, Pd, etc.)[8] halides with perovskite and nonperovskite structures, lead halide materials exhibit excellent properties, which essentially originate from the electronic structure of the Pb lone-pair $6s^2$ state.[9] However, the environmental toxicity of the crucial element Pb remains a limitation for large-scale commercialization.[10]

Recently, a novel all-inorganic copper halide CsCu₂I₃ with 1D architecture and soft crystal lattice, enabling strong self-trapped excitons and high photoluminescence quantum yield, has been reported to be a prospective self-activated luminescent material.[11] However, this material is rarely explored in photodetector applications, especially in high-crystalline form studying the underlying relationship between photoelectric performance and electronic structure. In addition, semiconductor single crystals with high phase purity, less grain boundaries and defects, which contribute to improving the figures of merit of the devices,[12] are more desirable than polycrystalline and amorphous materials for both fundamental and applied investigations in optoelectronics.[13] Meanwhile, single crystal platform is suitable for observing facet-dependent photophysical

Dr. Z. Q. Li, Dr. Z. L. Li, Prof. X. S. Fang
Department of Materials Science
Fudan University
Shanghai 200433, P. R. China
E-mail: xshfang@fudan.edu.cn
Prof. Z. F. Shi
Key Laboratory of Materials Physics of Ministry of Education
School of Physics and Microelectronics
Zhengzhou University
Daxue Road 75, Zhengzhou 450052, P. R. China
E-mail: shizf@zzu.edu.cn

The ORCID identification number(s) for the author(s) of this article can be found under https://doi.org/10.1002/adfm.202002634.

2002634 (1 of 10)

performances deriving from intrinsic structural anisotropy, which is intriguing for potential optoelectronic application.[14]

This paper first describes a fast speed, facet-dependent and broadband photodetector based on all-inorganic lead-free 1D $CsCu_2I_3$ single crystal, obtained through low-cost solution-processed antisolvent vapor assisted method. The fast carrier transport mobility, facet-dependent photoelectric performance and high stability of $CsCu_2I_3$ single crystal are mostly ascribed to 1D crystal structure and 1D electronic structure. The results show that the structurally low-dimensional metal halide single crystal with favorable crystal orientation and regulated electron transport is enabled to establish high-performance photodetector.

2. Results and Discussion

2.1. Crystal Growth and Crystalline Quality

$CsCu_2I_3$ single crystals are successfully prepared by a solution-processed growth method, which is described in detail in the Experimental Section. **Figure 1**a shows the photograph of freshly as-grown single crystals, whose powder X-ray diffraction (XRD) pattern with whole range of 10°–90° is depicted in Figure 1b. The XRD pattern exhibits weak noise background and strong signal peaks, whose position and intensity are in good agreement with those of crystal planes of the orthorhombic $CsCu_2I_3$ (PDF No. 01-072-9857, space group *Cmcm*). Visible rod-shaped morphology of 0.3–1.0 mm width and 1.5–6.0 mm length is clearly seen in the optical microscopy image of these single crystals in Figure 1c. To further check the crystalline quality, XRD measurements are conducted on different crystal planes

of an individual single crystal. As shown in Figure 1d, XRD pattern exhibits a series of strong diffraction peaks at 2θ of 10.8°, 21.6°, 32.7°, and 44.1°, which are corresponding to (110), (220), (330), (440) crystal planes, respectively. As shown in Figure 1e, XRD pattern shows several diffraction peaks at 2θ of 13.5°, 27.0°, 41.1°, 55.8°, and 71.6°, which are corresponding to (020), (040), (060), (080), and (0100) crystal planes, respectively. The strong noise background from {010} crystal planes are ascribed to the small area for X-ray irradiation. These XRD results reveal high crystalline quality and phase purity for $CsCu_2I_3$ single crystal,[15] whose morphology includes the {110} and {010} crystal planes.

2.2. Facet-Dependent Photoelectric Performance

The equilibrium morphology is a good reflection of inner crystal structure.[16] Therefore, the predicted morphology of $CsCu_2I_3$ single crystal is established using Bravais–Friedel and Donnay–Harker (BFDH) methods,[17] which is based on its known structure parameters. As seen in Figure S1 in the Supporting Information, the predicted morphology exhibits the {010}, {110}, {021}, {111} facets. It is worth noting that {111} facets are predicted but not experimentally observed, because the crystal morphology is also affected by kinetic factors.[18] Optical microscopy images of side view of several $CsCu_2I_3$ single crystals (perpendicular to the viewing surface) with parallel hexagon morphology are provided under bright background (Figure S2a–c, Supporting Information) and dark background (Figure S2d–f, Supporting Information), with the corresponding morphological schematic views (Figure S2g–i, Supporting Information) completely marked by crystal plane
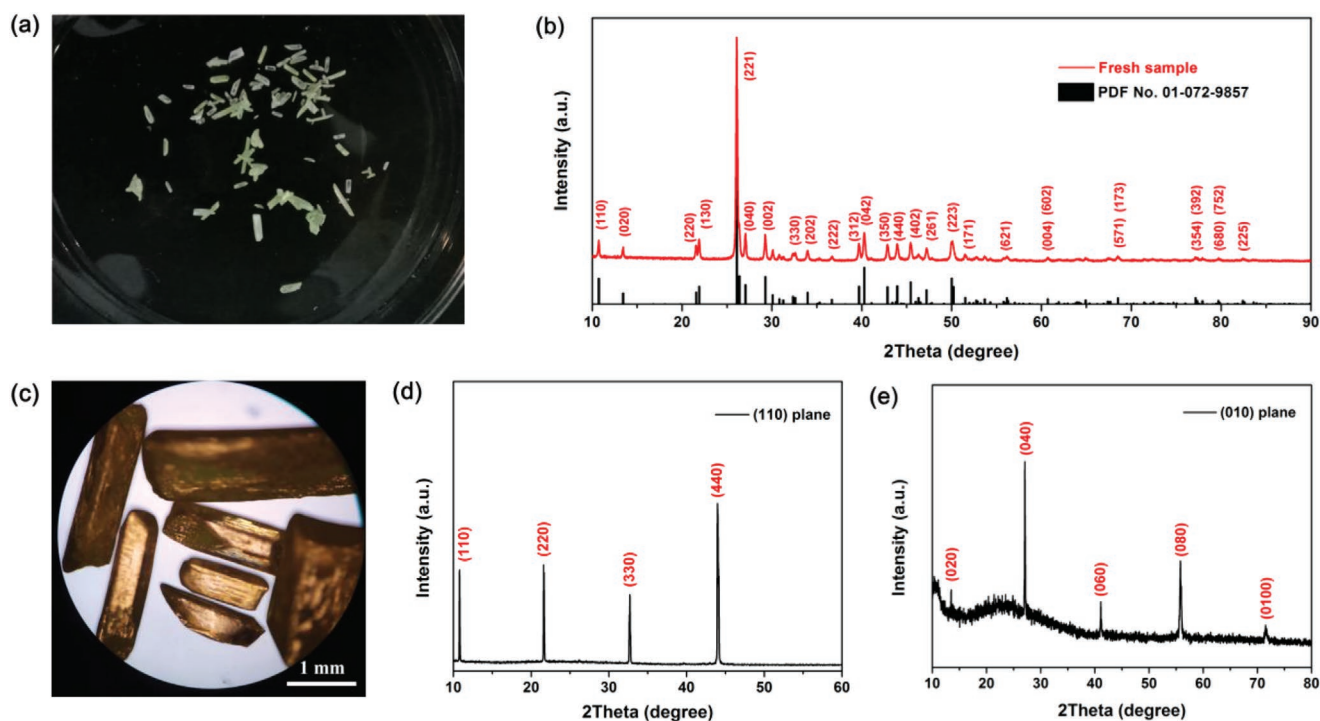

Figure 1. Crystal growth of $CsCu_2I_3$: a) Photograph of the freshly as-grown single crystals. b) Powder X-ray diffraction pattern. c) Optical microscopy image of the single crystals. d) X-ray diffraction pattern of the (110) plane. e) X-ray diffraction pattern of the (010) plane.
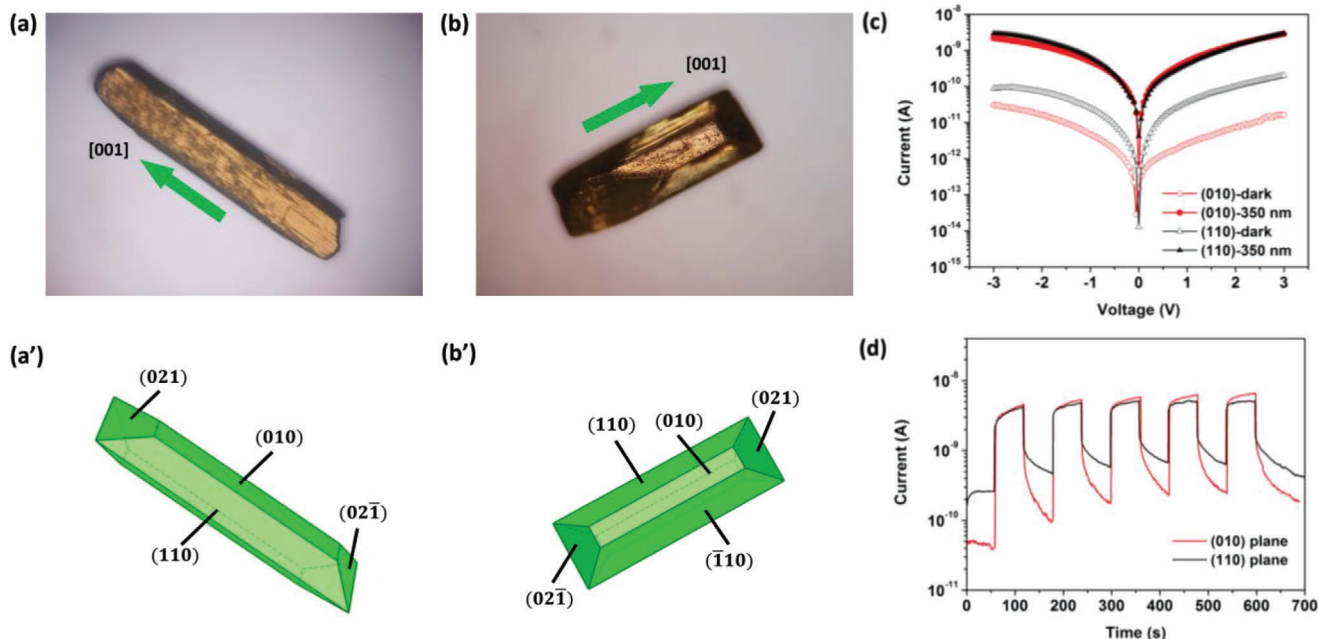
Figure 2. a,b) Optical microscopy images of CsCu$_2$I$_3$ single crystals with rod-shaped morphology. a',b') Schematic view of the corresponding crystal morphology. Comparison of photoelectric properties between (110) and (010) crystal planes of CsCu$_2$I$_3$ single crystals: c) I–V curves and d) I–t curves under dark and 350 nm illumination at 3 V bias.

indices. Combined with the results from XRD, it is concluded that the whole morphology of CsCu$_2$I$_3$ single crystal consists of totally {010}, {110}, and {021} ten crystal planes, where {010} crystal planes include (010) and (0$\bar{1}$0) two crystal planes, {110} crystal planes include (110), (1$\bar{1}$0), ($\bar{1}$10), and ($\bar{1}\bar{1}$0) four crystal planes, {021} crystal planes include (021), (0$\bar{2}$1), (02$\bar{1}$), and (0$\bar{2}\bar{1}$) four crystal planes.

In order to study the facet-dependent photoresponse of CsCu$_2$I$_3$ single crystal, (010) and (110) crystal planes parallel to the viewing surface (shown in **Figure 2**a,b) are selected to perform photoelectric performances, with the corresponding morphological schematic views shown in Figure 2a',b'. As I–V curves at the voltage from −3 V to 3 V shown in Figure 2c, the dark current of (010) crystal plane is lower than that of (110) crystal plane, while the photocurrent of (010) crystal plane is close to that of (110) crystal plane under 350 nm illumination. As shown in Figure 2d, I–t curves at the voltage of 3 V also reveal that the dark current of (010) crystal plane is lower than that of (110) crystal plane, while the photocurrent of (010) crystal plane is close to that of (110) crystal plane under 350 nm illumination. To further confirm this observation, more samples are employed for the identical I–V measurements targeting at (010) and (110) crystal planes of CsCu$_2$I$_3$ single crystal, as shown in Figure S3 in the Supporting Information. Although the photocurrent at the voltage of 3 V varies around 1.9–6.0 nA for both two crystal planes, (010) crystal planes show dark currents of 0.03–0.05 nA, which are much lower than those of (110) crystal planes (more than 0.1 nA). The photoresponse data of I–V curves at 3 V from Figure S3 in the Supporting Information are clearly collected in Table S1 in the Supporting Information. These results indicate that the {010} crystal plane has better photoelectric performances, and its higher on–off ratio is mainly due to its much lower dark current.

2.3. Application in Photodetector

The photoelectric performances of metal–semiconductor–metal (MSM) photodetector, based on the {010} crystal plane of an individual CsCu$_2$I$_3$ single crystal, is systematically investigated, with the schematic diagram depicted in **Figure 3**a. A monochromator-filtered continuous tunable Xe-lamp is adopted as the light source, and its relationship between wavelength and photodensity is provided in Figure S4 in the Supporting Information. Figure 3b describes the semilogarithmic I–V curves with characteristics of asymmetric dark current and symmetric photocurrent at forward and reverse bias, under dark condition and broadband illumination from 250 nm to 500 nm. The adoption of symmetric Ag electrodes form Schottky contacts with CsCu$_2$I$_3$ single crystal, which are verified from the nonlinear characteristics of I–V curves (Inset in Figure 3b). At 3 V bias, the device yields a dark current of 0.016 nA, while the highest photocurrent of 3.0 nA is achieved at 350 nm, with on–off ratio reaching a climax of 188. The on–off ratio of CsCu$_2$I$_3$ single crystal is much higher than those of most photodetectors based on individual all-inorganic lead-free metal halide.[24,44] It is noted that potential photocurrents are observed under 0 V, corresponding to the displayed open-circuit voltage (V$_{oc}$) of 0.05 V and photovoltaic self-powered performance from the Schottky barriers.[19]

To study the response speed and device stability, the dynamic time-dependent photocurrent of the photodetector is tested upon 350 nm illumination. Figure 3c presents I–t curves with several on–off cycles under six different bias voltages of 0–9 V. As bias voltage increases, the on–off ratio decreases due to the increased dark current. The prepared photodetector at 3 V bias demonstrates a lower dark current at the beginning, and then reaches
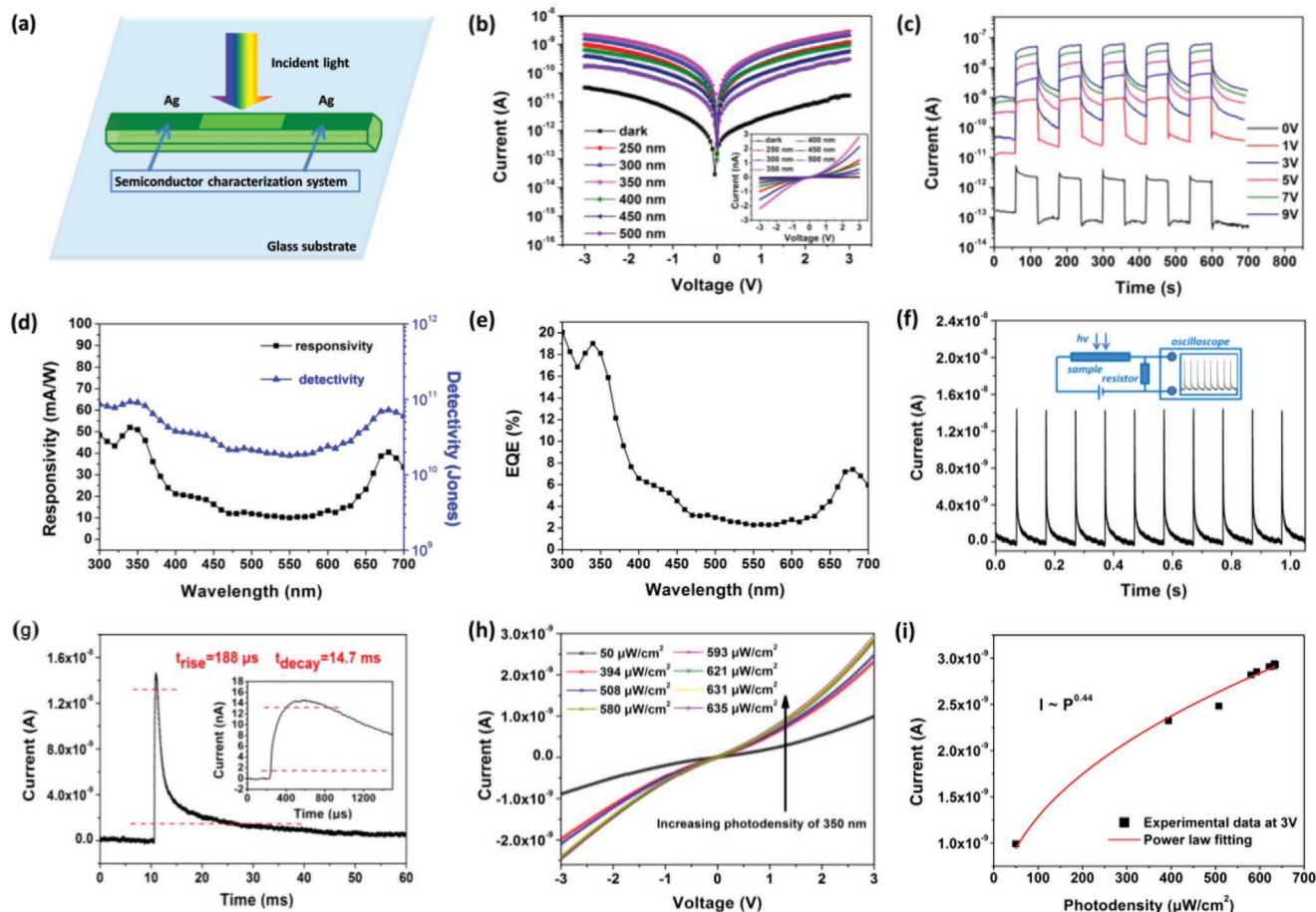
Figure 3. Photoelectric performances of CsCu$_2$I$_3$ photodetector on (010) plane: a) Schematic diagram of the CsCu$_2$I$_3$ photodetector. b) I–V curves under dark and illumination of 250–500 nm. c) I–t curves under 350 nm illumination at 0–9 V bias. d) Calculated responsivity and detectivity curves of 300–700 nm at 3 V bias. e) Calculated EQE curve of 300–700 nm at 3 V. f) Photoresponse to 10 Hz 355 nm laser pulse at 10 V bias. g) Estimated rise and decay time from single pulse response curve, the inset is the enlarged curve. h) Light intensity-dependent I–V curves under 350 nm illumination. i) Photocurrent as a function of photodensity and the corresponding power law fitting curves under 350 nm illumination at 3 V bias.

a stable dark current of 0.2 nA and photocurrent of around 6.0 nA for several on–off repetitions. Compared to the data obtained from I–V curves, the higher dark current and photocurrent are mainly resulted from the light-induced resistance reduce of CsCu$_2$I$_3$ single crystal according to the photoconductive phenomenon,[20] which is confirmed by photocurrent enhancement during lasting illumination. After removing the bias voltage, the light-induced pyroelectric effect is also observed from the signals of a sharp rising edge, a stable plateau and a sharp falling edge in each on–off cycle,[21] which is more clearly shown in Figure S5 in the Supporting Information. Therefore, the sensitive photocurrent of CsCu$_2$I$_3$ single crystal is a complicated process combining photoconductive and photovoltaic–pyroelectric effects.[22]

Considering the influences of effective illumination area S and incident light power density P_λ (subscripted λ is the illumination wavelength) on the photocurrent, the responsivity R_λ is introduced to evaluate the sensitivity of photodetector,[23] as defined by the following formula

$$R_\lambda = \frac{I_{ph} - I_{dark}}{P_\lambda S} \tag{1}$$

where I_{ph} is the photocurrent of photodetector, I_{dark} is the dark current of photodetector. As low dark current is expected to obtain high sensitivity to weak light signal,[23] the detectivity D^* is calculated as follows

$$D^* = \frac{R_\lambda}{(2e\,I_{dark}/S)^{1/2}} \tag{2}$$

where e represents the elementary charge. Fixing bias voltage at 3 V, the photocurrents as a function of light wavelength are described by I–t test in Figure S6 in the Supporting Information. The effective illumination area S of the device is calculated as 0.02 mm^2 in Figure S7 in the Supporting Information. As shown in Figure 3d, the photodetector demonstrates UV-to-visible broadband (300–700 nm) photoresponse with the responsivity of 10.0–52.0 mA W^{-1} and the detectivity of (1.8–9.3) × 10^{10} Jones, which are much higher than the performances of most photodetectors based on Ag, Bi, Sn halides.[24] And the maximum and minimum values locate at 340 and 550 nm, respectively. External quantum efficiency (EQE) is another important parameter for evaluating photoelectric

conversion efficiency of the photodetector,[23] which is expressed as the equation

$$EQE = \frac{hc}{e} \frac{R_\lambda}{\lambda} \qquad (3)$$

where h is the Plank constant, c is the velocity of light, λ is the illumination wavelength. The EQE of this photodetector reaches 19% at 340 nm, and then decrease to 2.3% at 550 nm, and finally rise to 7.4% at 680 nm, as shown in Figure 3e.

The response time limitation of semiconductor characterization system is responsible for the obvious gap near rising and falling edge in Figure S5 in the Supporting Information, therefore, Q-switch Nd:YAG laser pulses and oscilloscope are introduced to trace the transient response time of the CsCu$_2$I$_3$ single crystal photodetector. Using 355 nm laser pulses with 10 Hz frequency and 10 V bias, the device demonstrates ultrafast, highly stable and repeatable photoresponse as displayed in Figure 3f. The time-resolved photoresponse of a single period is clearly shown in Figure 3g, and the rise time from 10% to 90% (based on signal maximum) is estimated to be 188 μs, the decay time from 90% to 10% is calculated to be 14.7 ms (inset in Figure 3g). Under lower bias voltages of 3 V, 5 V, 7 V, the fast rise and decay time are estimated within 0.25 ms and 20 ms (shown in Figure S8 in the Supporting Information). **Table 1** summarizes the photoelectric performances of typical photodetectors based on all-inorganic lead-free metal halide with perovskite and nonperovskite structures under air atmosphere and room temperature, and 1D CsCu$_2$I$_3$ single crystal photodetector demonstrates much faster response time than most photodetectors, especially the fastest rise time.

The generation probability of light-induced carrier is directly proportional to the absorbed photon flux, and the photocurrent is described as a function of photodensity according to the power law: $I = \alpha P^\theta$, where α is a constant under a given wavelength. Figure 3h displays nonlinear I–V curves of the CsCu$_2$I$_3$ single crystal photodetector under 350 nm illumination and varying light intensities. Through fitting the curve in Figure 3i with the power law equation, θ is calculated to be 0.44 at 3 V bias. To further examine the fitting accuracy, θ is fitted to be 0.47 and 0.44 at 1 V and 2 V bias, as shown in Figure S9 in the Supporting Information. It is suggested that the nonunity exponent θ indicates complex processes of electron–hole generation, trapping, and recombination for CsCu$_2$I$_3$ single crystal.[25]

2.4. Air Stability

Long-term air stability of CsCu$_2$I$_3$ single crystal, which is essential for photodetectors, is examined by powder XRD and X-ray photoelectron spectroscopy (XPS). **Figure 4**a presents highly matched XRD curves from samples exposed to the open air for 25 and 45 days, respectively. This result indicates that CsCu$_2$I$_3$ single crystal maintains high phase purity and crystalline quality under open air atmosphere (at least 70%RH moisture). All peaks are classified as main constituent elements (Cs, Cu, and I) of CsCu$_2$I$_3$ single crystal (exposed to open air for 40 days) from survey X-ray photoelectron spectrum in Figure 4b, except for C 1s and O 1s peaks from absorbed contaminations. Figure 4c–e displays high-resolution X-ray photoelectron spectra for Cs 3d, Cu 2p, and I 3d core levels, which are doublet peaks with the spin–orbit coupling separation of 14.0, 19.8, and 11.4 eV (coincide with the values in ref. [26]), respectively. Cs 3d$_{5/2}$ core level is located at the peak of 724.6 eV, while Cs 3d$_{3/2}$ core level at 738.6 eV is overlapped by I MNN auger lines (at

Table 1. Photoelectric performances and material descriptions of typical photodetectors based on all-inorganic lead-free metal halide perovskites and nonperovskites under air atmosphere and room temperature.

Photodetector	Material description				Λ [nm]	P_λ [mW cm^{-2}]	Bias [V]	I_{ph} [nA]	I_{dark} [nA]	Response time		Refs.
	Type	D$_1$[a]	D$_2$[b]	MHP[c]						t_{rise} [ms]	t_{decay} [ms]	
Ti/Au-CsYbI$_3$/grapheme-Ti/Au	Hybrid film	3D	3D	Y	400	–	–	–	–	694	4648	[38]
Au-CsSnBr$_{1.5}$Cl$_{1.5}$-Au	Polycrystalline powder	3D	3D	Y	445	–	0.1	44.3	4.94	–	–	[24a]
ITO-Cs$_3$Cu$_2$I$_5$-ITO	Polycrystalline film	0D	0D	N	265	2.74	0	0.14	0.0011	26.2	49.9	[39]
Au-CsBi$_3$I$_{10}$-Au	Polycrystalline film	3D	0D	Y	650	84	1	11.8	0.00016	0.33	0.38	[40]
ITO-Cs$_2$AgBiBr$_6$/SnO$_2$-Au	Heterojunction film	3D	<3D	Y	350	100	0	–	–	<3	<3	[41]
In-Cs$_2$AgBiBr$_6$/GaN-Ag	Heterojunction film	3D	<3D	Y	265	2.4	0	7[d]	0.01[d]	3.463	8.442	[42]
Ti/Au-CsSnI$_3$-Ti/Au[e]	Nanowire array	3D	3D	Y	940	50	0.1	6800	6300	83.8	243.4	[24f]
ITO-Cs$_3$Bi$_2$I$_9$-ITO[e]	Nanoplate	2D	2D	Y	450	228.08	8	0.14[d]	<0.05	10.2	37.2	[24e]
Ti/Au-Cs$_3$Sb$_2$Br$_9$-Ti/Au	Nanoflake	2D	2D	Y	450	–	10	3[d]	–	48	24	[43]
Au/Cs$_3$Sb$_2$Cl$_9$/Au	Nanowire	2D	2D	Y	410	–	0.9	18000[d]	3000[d]	130	230	[44]
Au-Cs$_2$AgInCl$_6$-Au	Single crystal	3D	<3D	Y	365	2.36	5	8	0.2[d]	2.11	–	[24d]
Au-Cs$_2$SnCl$_6$-xBrx-Au	Single crystal	0D	0D	N	590	1.27	−20	−0.19[d]	−0.01[d]	4.34	–	[24c]
Ag-Cs$_2$AgBiBr$_6$-Ag	Single crystal	3D	<3D	Y	400	66.3	5	38[d]	0.7[d]	159	85	[24b]
Ag-CsCu$_2$I$_3$-Ag	Single crystal	1D	1D	N	350	0.6	3	6.3	0.2	<0.25	<20	this work

[a]D$_1$ = dimensionality of crystal structure; [b]D$_2$ = dimensionality of electronic structure; [c]MHP = metal halide perovskite, "Y = yes" means the material belong to metal halide perovskite, "N = no" means the material belong to metal halide nonperovskite; [d]The data are calculated from the I–V or I–t curves in references; [e]The photoelectric measurements were carried out under vacuum.
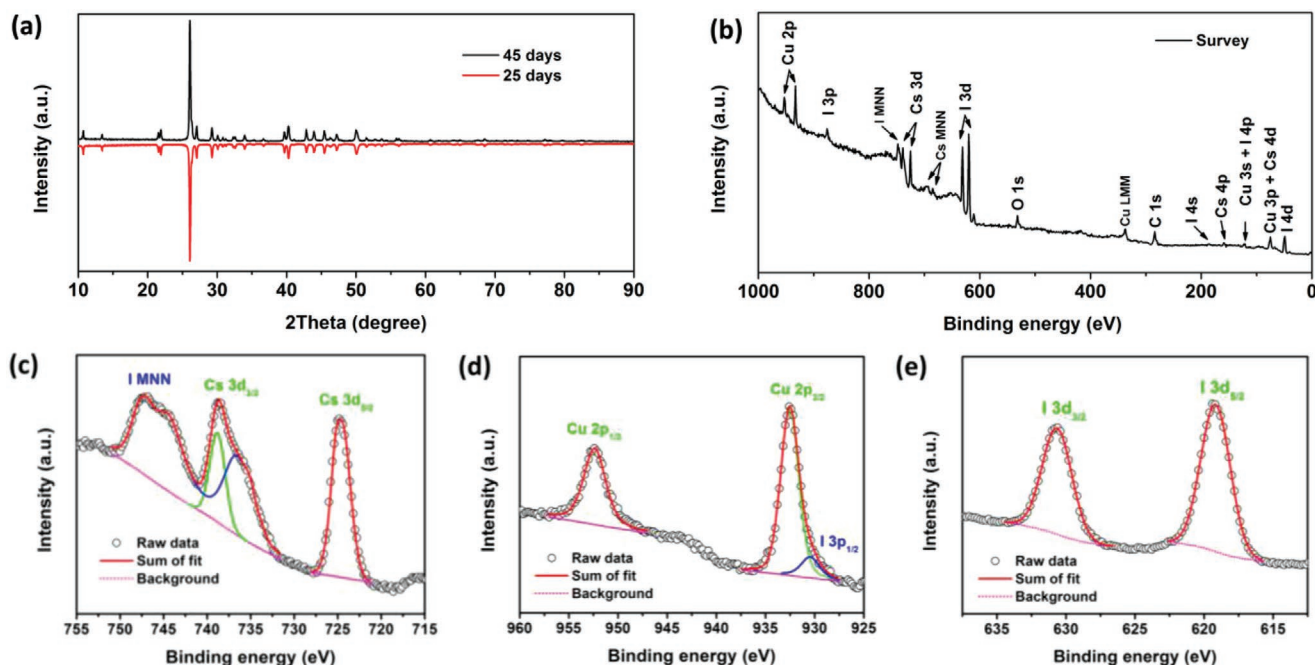
Figure 4. Air stability of CsCu$_2$I$_3$ single crystals under ambient atmosphere: a) Powder X-ray diffraction patterns of CsCu$_2$I$_3$ single crystals exposed to open air for 25 and 45 days. b) Survey spectrum and high-resolution X-ray photoelectron spectra. c) Cs 3d core level, d) Cu 2p core level, e) I 3d core level of CsCu$_2$I$_3$ single crystals exposed to open air for 40 days.

around 748.0 eV and 738.0 eV),[26] which are produced under Mg Kα irradiation. The asymmetric peak is deconvoluted with two peaks at 932.4 eV and 930.5 eV, which are ascribed to Cu 2p$_{3/2}$ and I 3p$_{1/2}$. The single peak of Cu 2p$_{3/2}$ and absence of Cu(II) satellite peaks indicate the monovalent Cu(I) in CsCu$_2$I$_3$ single crystal.[27] Both peaks of I 3d$_{5/2}$ and I 3d$_{3/2}$ core levels are symmetric at 619.2 eV and 630.6 eV, respectively. These results provide the evidence of high stability of monovalent Cs, Cu and I in CsCu$_2$I$_3$ single crystal under open air atmosphere, which is meaningful to long-term application of CsCu$_2$I$_3$ single crystal photodetector.

2.5. Structure–Property Relationship

To gain insights into structural origins of the high performance of CsCu$_2$I$_3$ single crystal, both 1D crystal structure and 1D electronic structure are discussed. From the view of crystal structure along crystallographic *c* direction in **Figure 5**a, the Cu(I) iodide wires are isolated by Cs atoms, forming 1D crystal structure along [001] direction. The configuration of single 1D Cu(I) iodide wire surrounded by Cs atoms is similar to core–shell structure,[11c] as shown in Figure 5b. There is obvious one type of Cs site, one type of Cu site and two different types of I sites in the framework. Due to the small ionic radius of Cu(I) and the high energy level for Cu 3d^{10} orbitals,[28] Cu(I) atoms energetically favor fourfold coordination to form [CuI$_4$] tetrahedra. The [CuI$_4$] tetrahedra constitutes a twofold chain through shared edges, which is clearly seen from [Cu$_2$I$_6$] dimer (two [CuI$_4$] tetrahedra with shared edge), as displayed in Figure 5c. The high stability of 1D CsCu$_2$I$_3$ single crystal originates from

the fourfold coordination environment of all Cu(I) atoms, while poor air and thermal stability are observed in 0D Cs$_3$Cu$_2$I$_5$, which contain both threefold and fourfold coordination environment of Cu(I) atoms.[28b]

Based on the 1D crystal structure, 1D electronic structure is formed accordingly in CsCu$_2$I$_3$ single crystal.[29] The density functional theory (DFT) calculation based on the primitive cell is conducted to examine the electronic structure of CsCu$_2$I$_3$, which has a direct optical band gap of 2.02 eV, as shown in **Figure 6**a. The valence band maximum (VBM) and conduction band minimum (CBM) are both located at G point (in reciprocal space). Highly dispersive bands near the valence and conduction edges endow metal halides with excellent carrier transport properties.[30] Both the VBM and CBM are most dispersive along [001] direction (G-Z, T-Y and S-R), indicating relatively small effective mass and high mobility of electrons and holes along the Cu(I) iodide wires. In contrast, perpendicular to the crystallographic c direction, the band along [010] direction (Z-T and Y-G) is more dispersive than that along [$\bar{1}$10] direction (G-S and R-Z), suggesting that {110} crystal planes have stronger confinement of electrons and holes than the {010} crystal planes, involving an anisotropic carrier transport performance in CsCu$_2$I$_3$ single crystal.[4b] The total and partial density of states (TDOS and PDOS) in Figure 6b indicate that the state near VBM are mainly contributed by Cu 3d and I 5p orbitals, while those near the CBM are constituted by Cu 4s and I 5s orbitals. Since the optical absorption of materials are considerably related to the electronic transitions close to the forbidden band,[31] the photoactive sites are isolated by Cs$^+$ ions in CsCu$_2$I$_3$, considering Cs$^+$ ions making few contributions to VBM and CBM.
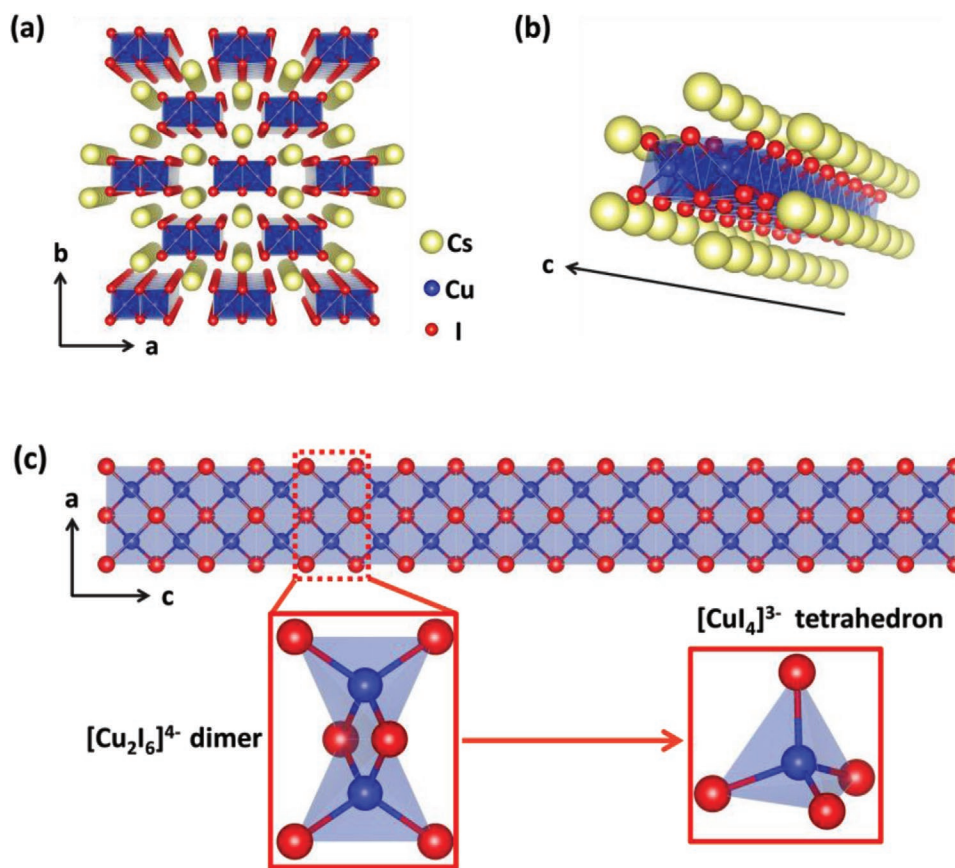
Figure 5. 1D crystal structure of $CsCu_2I_3$ single crystal: a) Perspective view of crystal structure along [001] direction. b) View of 1D Cu(I) iodide wire surrounded by Cs atoms. c) $[Cu_2I_6]$ dimer and $[CuI_4]$ tetrahedron.

From the calculated 3D electron density difference (EDD) plot in the a–b plane (Figure 6c), the accumulation and depletion of electrons are mainly around Cu−I bonds, indicating 1D electronic distribution around the Cu(I) iodide wires. The 1D electronic distribution preference is obviously seen in the calculated EDD plots from different perspectives (slices 1–7 in Figure S10a,c,d, Supporting Information) in Figure 6d–f, including the plane close to {110} crystal plane and across Cu,I atoms (slices 1,2 in Figure S10a, Supporting Information), the a–c plane across Cu atoms (slice 3 in Figure S10c, Supporting Information), the a–b plane across Cu atoms (slice 7 in Figure S10d, Supporting Information). The electron localization function (ELF) is helpful to analyze the localization characteristics of electrons.[32] The calculated ELF plots from different perspectives are shown in Figure 6g–i and Figure S10b, e–g in the Supporting Information. It is worth noting that the Cu−I bonds show non-negligible covalent characteristics, which are similar to CuI.[33] The electron density of {110} crystal planes (in Figure 6g and Figure S10b in the Supporting Information, the overall area mean ELF values is 0.44) is higher than that of {010} crystal planes (Figure 6h, the overall area mean ELF values is 0.24), corresponding to higher dark current in {110} crystal planes. Above all, it is speculated that photogenerated electrons are localized in the twofold chain created by [CuI4] tetrahedra, leading to the fast transport mobility among the chain, which is parallel to [001] direction.

3. Conclusion

$CsCu_2I_3$ single crystal, with high crystalline quality, visible shape, and millimeter size, is successfully grown by low-cost solution-processed method. Its whole morphology is revealed by theoretical BFDH simulation and experimental X-ray diffraction methods, including totally {010}, {110}, and {021} facets. Facet-dependent photoresponse of $CsCu_2I_3$ single crystal demonstrates that the on–off ratio of {010} crystal plane is higher than that of {110} crystal plane. For the first time, the photoelectric performances of the $CsCu_2I_3$ single crystal photodetector are systematically investigated. This device exhibits stable and UV-to-visible broadband (300–700 nm) photoresponse, including a responsivity of 10.0–52.0 mA W^{-1}, a detectivity of $(1.8–9.3) \times 10^{10}$ Jones and an EQE of 2.3–19% (3 V bias), as well as fast response time ($t_{rise} = 0.19$ ms, $t_{decay} = 14.7$ ms, at 350 nm and 10 V bias), outperforming most reported photodetectors based on all-inorganic lead-free metal halides. The high stability of monovalent Cs, Cu, and I in $CsCu_2I_3$ single crystal, which originates from fourfold coordination [CuI4] tetrahedra, is meaningful for long-term optoelectronic application under open air. Through DFT calculation, it is confirmed that carriers with relatively small effective mass and high mobility transport along the 1D Cu(I) iodide wires. It is speculated that photogenerated electrons are localized in the twofold chain created by [CuI4] tetrahedra, leading to the fast transport mobility
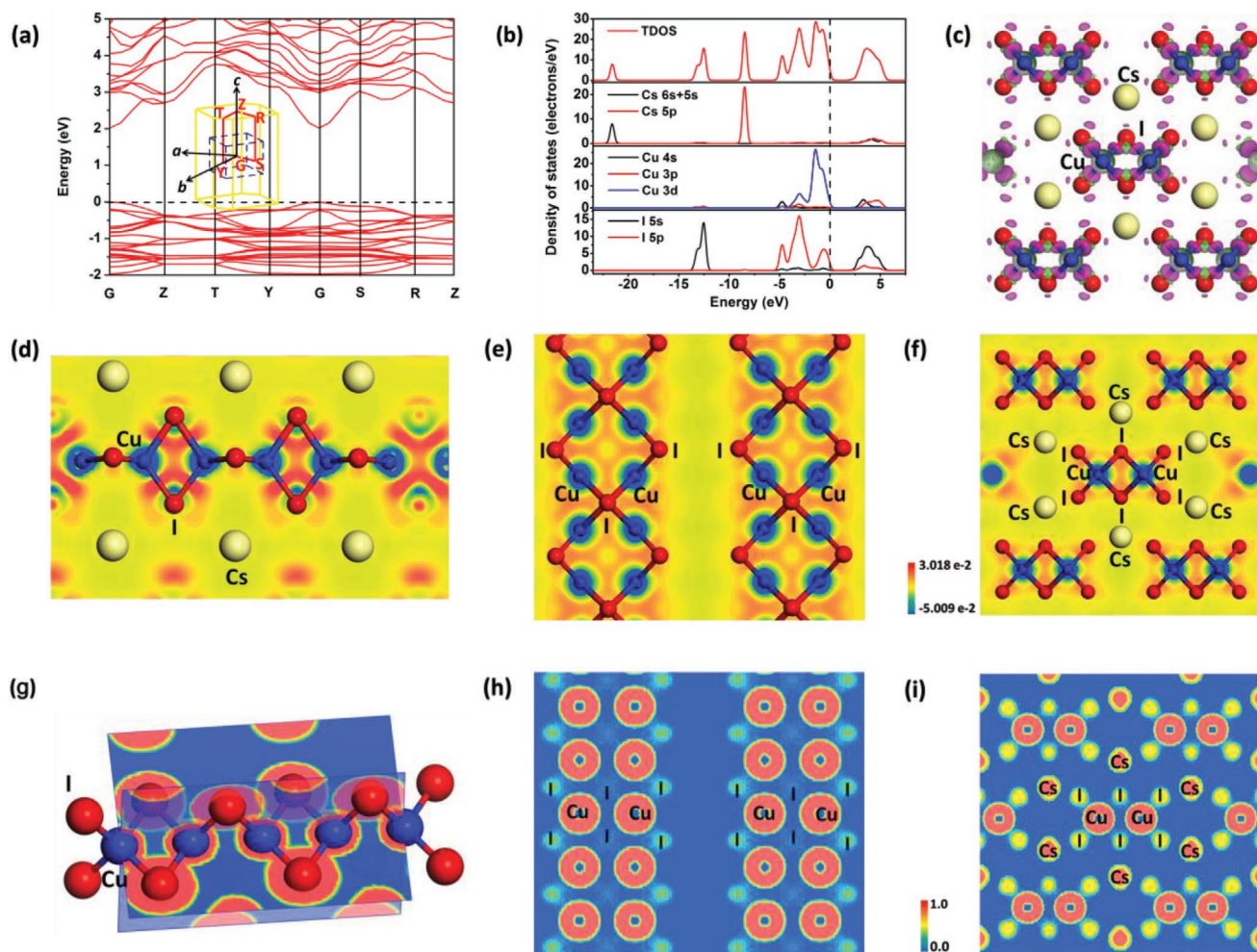
**ADVANCED
SCIENCE NEWS**
www.advancedsciencenews.com

**ADVANCED
FUNCTIONAL
MATERIALS**
www.afm-journal.de

Figure 6. 1D electronic structure of CsCu$_2$I$_3$ single crystal: a) Calculated electronic band structure along G-Z-T-Y-G-S-R-Z path throughout the Brillouin zone as depicted in the inset. b) Calculated total and partial DOS, dashed line represents Fermi level set at 0.0 eV. c) Side view of the 3D EDD plot in the a–b plane. Pink and green isosurfaces denote electron accumulation and depletion regions with a value of 0.026 e Å^{-3}, respectively. Calculated EDD plots from different perspectives: d) The plane close to {110} crystal planes and across Cu,I atoms, e) the a–c plane across Cu atoms, f) the a–b plane across Cu atoms. Calculated ELF plots from different perspectives: g) Two planes close to {110} crystal planes and across Cu,I atoms on single Cu(I) iodide wire, h) the a–c plane across Cu atoms, i) the a–b plane across Cu atoms.

among the twofold chain. Meanwhile, {110} crystal plane has stronger confinement of electrons and holes than the {010} crystal plane, involving an anisotropic carrier transport performance in CsCu$_2$I$_3$ single crystal. The electron density of {110} crystal plane is higher than that of {010} crystal plane, corresponding to higher dark current in {110} crystal plane. This work not only demonstrates a high-performance photodetector based on 1D CsCu$_2$I$_3$ single crystal, but also provides insights into its 1D electronic structure, promoting the development of high-performance optoelectronics based on nontoxic and stable low-dimensional metal halides in the future.

4. Experimental Section

Crystal Growth: CsCu$_2$I$_3$ single crystal was grown by antisolvent vapor assisted method,[11c] the detailed process is depicted as follows. The raw materials 1.299 g CsI (Aladdin Chemistry Co., Ltd., 99.999%) and 0.952 g CuI (Aladdin Chemistry Co., Ltd., 99.95%) were dissolved in the solvent

mixed with 1 mL dimethyl sulfoxide (Sinopharm Chemical Reagent Co., Ltd., DMSO, 99.0%) and 4 mL *N,N*-dimethylformamide (Aladdin Chemistry Co., Ltd., DMF, 99.8%). The mixture was constantly stirred at 60 °C until clear solution was obtained. The methanol anhydrous (Sinopharm Chemical Reagent Co., Ltd., 99.5%) was dropwise added to the solution until white precipitate did not disappear. Immediately, the precipitate was removed by filters and syringes, and the saturation solution was transferred to a small vial. This vial was placed in a large vial, which contained methanol anhydrous and was finally sealed by paraffin film. The whole apparatus was standing on a 60 °C hot plate for three days. At the end of growth, CsCu$_2$I$_3$ single crystals were cleaned using ethyl alcohol (Sinopharm Chemical Reagent Co., Ltd., 95%) and *n*-hexane (Sinopharm Chemical Reagent Co., Ltd., 95%) from the bottom of vial.

Material Characterization: X-ray diffraction patterns were collected using Bruker D8 Advance X-ray diffractometer equipped with Cu Kα radiation (λ = 0.15406 nm). The powder sample was tested with the scan step of 0.02° and a step time of 1 s, and the bulk crystal sample was tested with the scan step of 0.02° and a step time of 0.2 s. X-ray photoelectron spectra were acquired by the PHI 5000C&PHI5300 X-ray photoelectron spectrometer, equipped with a dual Mg/Al anode. All peaks were calibrated using the C 1s peak (284.6 eV) as the reference,

and the deconvolution was conducted using a Gaussian–Lorentzian fitting after background subtraction. The optical photographs were obtained by Olympus optical microscope. Crystal structure analysis was performed through Vesta 3.4.4,[34] based on the crystallographic information file (CIF) data of $CsCu_2I_3$ single crystal.[35]

Device Construction: A single crystal was fixed on glass substrate to facilitate the photoelectric measurements, with the desired crystal plane parallel to its surface. A couple of silver pastes with sub-millimeters apart were deposited on one crystal plane as electrodes. The crystal plane orientation ({110} and {010} planes) was determined by observing crystal plane angle (two types of angles calculated to be 128.6° and 102.7° in Figure S2, Supporting Information).

Photoelectric Measurements: A 75 W Xe lamp equipped with a monochromator was utilized as light source system. The photodensity was detected using optical power meter (Ophir NOVA II). The I–V and I–t characteristics were collected through the semiconductor characterization system (Keithley 4200-SCS). The transient photoresponse was recorded using the Q-switch Nd:YAG laser (Continuum Electro-Optics, MINILITE II), connecting with the resistor and the oscilloscope (Tektronix MSO/DPO5000). All measurements were conducted under air atmosphere and room temperature.

Electronic Structure Calculations: Based on the density function theory (DFT), first-principle calculation was executed using the plane-wave pseudopotential method through Cambridge sequential total energy package (CASTEP) code.[36] Structural parameters of $CsCu_2I_3$ single crystal were used for the calculation. The generalized gradient approximation (GGA) with Perdew–Burke–Ernzerhof (PBE) was introduced to describe the exchange-correlation potential for electron interactions.[37] The pseudo atomic calculations were carried out for the valence electrons of all constituent elements, including $Cs\ 5s^2\ 5p^6\ 6s^1$, $Cu\ 3p^6\ 3d^{10}\ 4s^1$, $I\ 5s^2\ 5p^5$. The plane-wave basis cut-off and energy convergence criterion were set as 400 eV and 10^{-5} eV, respectively. The Brillouin zone sampling was carried out in a $3 \times 3 \times 4$ Monkhorst–Pack k-point grid.

Supporting Information

Supporting Information is available from the Wiley Online Library or from the author.

Conflict of Interest

The authors declare no conflict of interest.

[1] H. Chen, H. Liu, Z. Zhang, K. Hu, X. S. Fang, *Adv. Mater.* **2016**, *28*, 403.

[2] a) D. B. Velusamy, M. A. Haque, M. R. Parida, F. Zhang, T. Wu, O. F. Mohammed, H. N. Alshareef, *Adv. Funct. Mater.* **2017**, *27*, 1605554; b) S. Y. Li, Y. Zhang, W. Yang, H. Liu, X. S. Fang, *Adv. Mater.* **2020**, *32*, 1905443; c) Z. H. Long, X. J. Xu, W. Yang, M. X. Hu, D. V. Shtansky, D. Golberg, X. S. Fang, *Adv. Electron. Mater.* **2020**, *6*, 1901048.

[3] a) L. Etgar, *Energy Environ. Sci.* **2018**, *11*, 234; b) W. Yu, F. Li, L. Yu, M. R. Niazi, Y. Zou, D. Corzo, A. Basu, C. Ma, S. Dey, M. L. Tietze, U. Buttner, X. Wang, Z. Wang, M. N. Hedhili, C. Guo, T. Wu, A. Amassian, *Nat. Commun.* **2018**, *9*, 5354.

[4] a) Y. Li, Z. F. Shi, W. Q. Liang, L. T. Wang, S. Li, F. Zhang, Z. Z. Ma, Y. Wang, Y. Z. Tian, D. Wu, X. J. Li, Y. Zhang, C. X. Shan, X. S. Fang, *Mater. Horiz.* **2020**, *7*, 530; b) Z. Xiao, W. Meng, J. Wang, D. B. Mitzi, Y. Yan, *Mater. Horiz.* **2017**, *4*, 206.

[5] a) Y. Zhang, W. X. Xu, X. J. Xu, J. Cai, W. Yang, X. S. Fang, *J. Phys. Chem. Lett.* **2019**, *10*, 836; b) Y. Zhang, S. Y. Li, W. Yang, M. K. Joshi, X. S. Fang, *J. Phys. Chem. Lett.* **2019**, *10*, 2400; c) Z. Fang, M. Shang, Y. Zheng, T. Zhang, Z. Du, G. Wang, X. Duan, K. C. Chou, C. H. Lin, W. Yang, X. Hou, T. Wu, *Mater. Horiz.* **2020**, *7*, 1042.

[6] C. Zhou, Y. Tian, M. Wang, A. Rose, T. Besara, N. K. Doyle, Z. Yuan, J. C. Wang, R. Clark, Y. Hu, T. Siegrist, S. Lin, B. Ma, *Angew. Chem., Int. Ed.* **2017**, *56*, 9018.

[7] P. Gao, A. R. Bin Mohd Yusoff, M. K. Nazeeruddin, *Nat. Commun.* **2018**, *9*, 5028.

[8] a) B. Saparov, J. P. Sun, W. Meng, Z. Xiao, H. S. Duan, O. Gunawan, D. Shin, I. G. Hill, Y. Yan, D. B. Mitzi, *Chem. Mater.* **2016**, *28*, 2315; b) N. Sakai, A. A. Haghighirad, M. R. Filip, P. K. Nayak, S. Nayak, A. Ramadan, Z. Wang, F. Giustino, H. J. Snaith, *J. Am. Chem. Soc.* **2017**, *139*, 6030.

[9] F. Jiang, D. Yang, Y. Jiang, T. Liu, X. Zhao, Y. Ming, B. Luo, F. Qin, J. Fan, H. Han, *J. Am. Chem. Soc.* **2018**, *140*, 1019.

[10] C. Wu, Q. Zhang, G. Liu, Z. Zhang, D. Wang, B. Qu, Z. Chen, L. Xiao, *Adv. Energy Mater.* **2020**, *10*, 1902496.

[11] a) Q. Li, Z. Chen, B. Yang, L. Tan, B. Xu, J. Han, Y. Zhao, J. Tang, Z. Quan, *J. Am. Chem. Soc.* **2020**, *142*, 1786; b) Y. Li, Z. F. Shi, L. Wang, Y. C. Chen, W. Liang, D. Wu, X. Li, Y. Zhang, C. X. Shan, X. S. Fang, *Mater. Horiz.* **2020**, https://doi.org/10.1039/D0MH00250J; c) R. Lin, Q. Guo, Q. Zhu, Y. Zhu, W. Zheng, F. Huang, *Adv. Mater.* **2019**, *31*, 1905079.

[12] W. Yuan, G. Niu, Y. Xian, H. Wu, H. Wang, H. Yin, P. Liu, W. Li, J. Fan, *Adv. Funct. Mater.* **2019**, *29*, 1900234.

[13] D. Shi, V. Adinolfi, R. Comin, M. Yuan, E. Alarousu, A. Buin, Y. Chen, S. Hoogland, A. Rothenberger, K. Katsiev, *Science* **2015**, *347*, 519.

[14] a) J. Duan, P. Huang, K. Liu, B. Jin, A. A. Suleiman, X. Zhang, X. Zhou, T. Zhai, *Adv. Funct. Mater.* **2019**, *29*, 1903216; b) D. Periyanagounder, T. C. Wei, T. Y. Li, C. H. Lin, T. P. Gonçalves, H. C. Fu, D. S. Tsai, J. J. Ke, H. W. Kuo, K. W. Huang, N. Lu, X. S. Fang, J. H. He, *Adv. Mater.* **2020**, *32*, 1904634.

[15] Z. Li, P. Zhu, J. Ding, N. Ji, Y. Chen, Z. Wang, X. Duan, H. Jiang, *Cryst. Growth Des.* **2019**, *19*, 7143.

[16] W. Kaminsky, *J. Appl. Crystallogr.* **2007**, *40*, 382.

[17] a) A. Bravais, *Etudes Cristallographiques*, Gauthier-Villars, Paris **1866**; b) G. Friedel, *Bull. Soc. Fr. Mineral.* **1907**, *30*, 326; c) J. D. H. Donnay, D. Harker, *Am. Mineral.* **1937**, *22*, 446.

[18] X. Liu, E. Boek, W. Briels, P. Bennema, *Nature* **1995**, *374*, 342.

[19] W. Yang, Y. Zhang, Y. Zhang, W. Deng, X. S. Fang, *Adv. Funct. Mater.* **2019**, *29*, 1905923.

[20] a) E. Oksenberg, E. Sanders, R. Popovitz-Biro, L. Houben, E. Joselevich, *Nano Lett.* **2018**, *18*, 424; b) E. Liu, M. Long, J. Zeng, W. Luo, Y. Wang, Y. Pan, W. Zhou, B. Wang, W. Hu, Z. Ni, *Adv. Funct. Mater.* **2016**, *26*, 1938.

[21] Z. Wang, R. Yu, C. Pan, Z. Li, J. Yang, F. Yi, Z. L. Wang, *Nat. Commun.* **2015**, *6*, 1.

[22] D. You, C. Xu, W. Zhang, J. Zhao, F. Qin, Z. Shi, *Nano Energy* **2019**, *62*, 310.

[23] F. Teng, K. Hu, W. Ouyang, X. S. Fang, *Adv. Mater.* **2018**, *30*, 1706262.

[24] a) Z. Hong, D. Tan, R. A. John, Y. K. E. Tay, Y. K. T. Ho, X. Zhao, T. C. Sum, N. Mathews, F. García, H. S. Soo, *iScience* **2019**, *16*, 312; b) Y. Dang, G. Tong, W. Song, Z. Liu, L. Qiu, L. K. Ono, Y. Qi, *J. Mater. Chem. C* **2020**, *8*, 276; c) J. Zhou, J. Luo, X. Rong, P. Wei, M. S. Molokeev, Y. Huang, J. Zhao, Q. Liu, X. Zhang, J. Tang, *Adv. Opt. Mater.* **2019**, *7*, 1900139; d) J. Luo, S. Li, H. Wu, Y. Zhou, Y. Li, J. Liu, J. Li, K. Li, F. Yi, G. Niu, *ACS Photonics* **2018**, *5*, 398; e) Z. Qi, X. Fu, T. Yang, D. Li, P. Fan, H. Li, F. Jiang, L. Li, Z. Luo, X. Zhuang, *Nano Res.* **2019**, *12*, 1894; f) M. Han, J. Sun, M. Peng, N. Han, Z. Chen, D. Liu, Y. Guo, S. Zhao, C. Shan, T. Xu, *J. Phys. Chem. C* **2019**, *123*, 17566.

[25] M. Hu, F. Teng, H. Chen, M. Jiang, Y. Gu, H. Lu, L. Hu, X. S. Fang, *Adv. Funct. Mater.* **2017**, *27*, 1704477.

[26] J. Moulder, W. Stickle, P. Sobol, K. Bomben, *Handbook of X-Ray Photoelectron Spectroscopy*, Perkin-Elmer Corporation, Eden Prairie, MN **1992**.

[27] J. Ghijsen, L.-H. Tjeng, J. van Elp, H. Eskes, J. Westerink, G. A. Sawatzky, M. T. Czyzyk, *Phys. Rev. B* **1988**, *38*, 11322.

[28] a) R. D. Shannon, *Acta Crystallogr. A* **1976**, *32*, 751; b) Z. Xiao, K. Z. Du, W. Meng, D. B. Mitzi, Y. Yan, *Angew. Chem., Int. Ed.* **2017**, *56*, 12107.

[29] T. Jun, K. Sim, S. Iimura, M. Sasase, H. Kamioka, J. Kim, H. Hosono, *Adv. Mater.* **2018**, *30*, 1804547.

[30] J. Li, Q. Yu, Y. He, C. C. Stoumpos, G. Niu, G. G. Trimarchi, H. Guo, G. Dong, D. Wang, L. Wang, *J. Am. Chem. Soc.* **2018**, *140*, 11085.

[31] M. H. Lee, C. H. Yang, J. H. Jan, *Phys. Rev. B* **2004**, *70*, 235110.

[32] A. D. Becke, K. E. Edgecombe, *J. Chem. Phys.* **1990**, *92*, 5397.

[33] P. S. Kumar, N. Kini, A. Umarji, C. Sunandana, *J. Mater. Sci.* **2006**, *41*, 3861.

[34] K. Momma, F. Izumi, *J. Appl. Crystallogr.* **2011**, *44*, 1272.

[35] N. Jouini, L. Guen, M. Tournoux, *Rev. Chim. Miner.* **1980**, *17*, 486.

[36] S. J. Clark, M. D. Segall, C. J. Pickard, P. J. Hasnip, M. I. Probert, K. Refson, M. C. Payne, *Z. Kristallogr.* **2005**, *220*, 567.

[37] a) J. P. Perdew, K. Burke, M. Ernzerhof, *Phys. Rev. Lett.* **1996**, *77*, 3865; b) R. Godby, M. Schlüter, L. Sham, *Phys. Rev. B* **1987**, *36*, 6497.

[38] B. J. Moon, S. J. Kim, S. Lee, A. Lee, H. Lee, D. S. Lee, T. W. Kim, S. K. Lee, S. Bae, S. H. Lee, *Adv. Mater.* **2019**, *31*, 1901716.

[39] Z. X. Zhang, C. Li, Y. Lu, X. W. Tong, F. X. Liang, X. Y. Zhao, D. Wu, C. Xie, L. B. Luo, *J. Phys. Chem. Lett.* **2019**, *10*, 5343.

[40] X. W. Tong, W. Y. Kong, Y. Y. Wang, J. M. Zhu, L. B. Luo, Z. H. Wang, *ACS Appl. Mater. Interfaces* **2017**, *9*, 18977.

[41] C. Wu, B. Du, W. Luo, Y. Liu, T. Li, D. Wang, X. Guo, H. Ting, Z. Fang, S. Wang, *Adv. Opt. Mater.* **2018**, *6*, 1800811.

[42] Y. Li, Z. Shi, L. Lei, S. Li, D. Yang, D. Wu, T. Xu, Y. Tian, Y. Lu, Y. Wang, *Adv. Mater. Interfaces* **2019**, *6*, 1900188.

[43] Z. Zheng, Q. Hu, H. Zhou, P. Luo, A. Nie, H. Zhu, L. Gan, F. Zhuge, Y. Ma, H. Song, *Nanoscale Horiz.* **2019**, *4*, 1372.

[44] B. Pradhan, G. S. Kumar, S. Sain, A. Dalui, U. K. Ghorai, S. K. Pradhan, S. Acharya, *Chem. Mater.* **2018**, *30*, 2135.